SANDIA REPORT

SAND97-0259 • UC-910
Unlimited Release
Printed May 1997

Materials and Corrosion Characterization Using the Confocal Resonator

Chris P. Tigges, N. Robert Sorensen, Vincent M. Hietala, Thomas A. Plut, Jon S. Martens

Prepared by
Sandia National Laboratories
Albuquerque, New Mexico 87185 and Livermore, California 94550

Sandia is a multiprogram laboratory operated by Sandia Corporation, a Lockheed Martin Company, for the United States Department of Energy under Contract DE-AC04-94AL85000.

Sandia National Laboratories

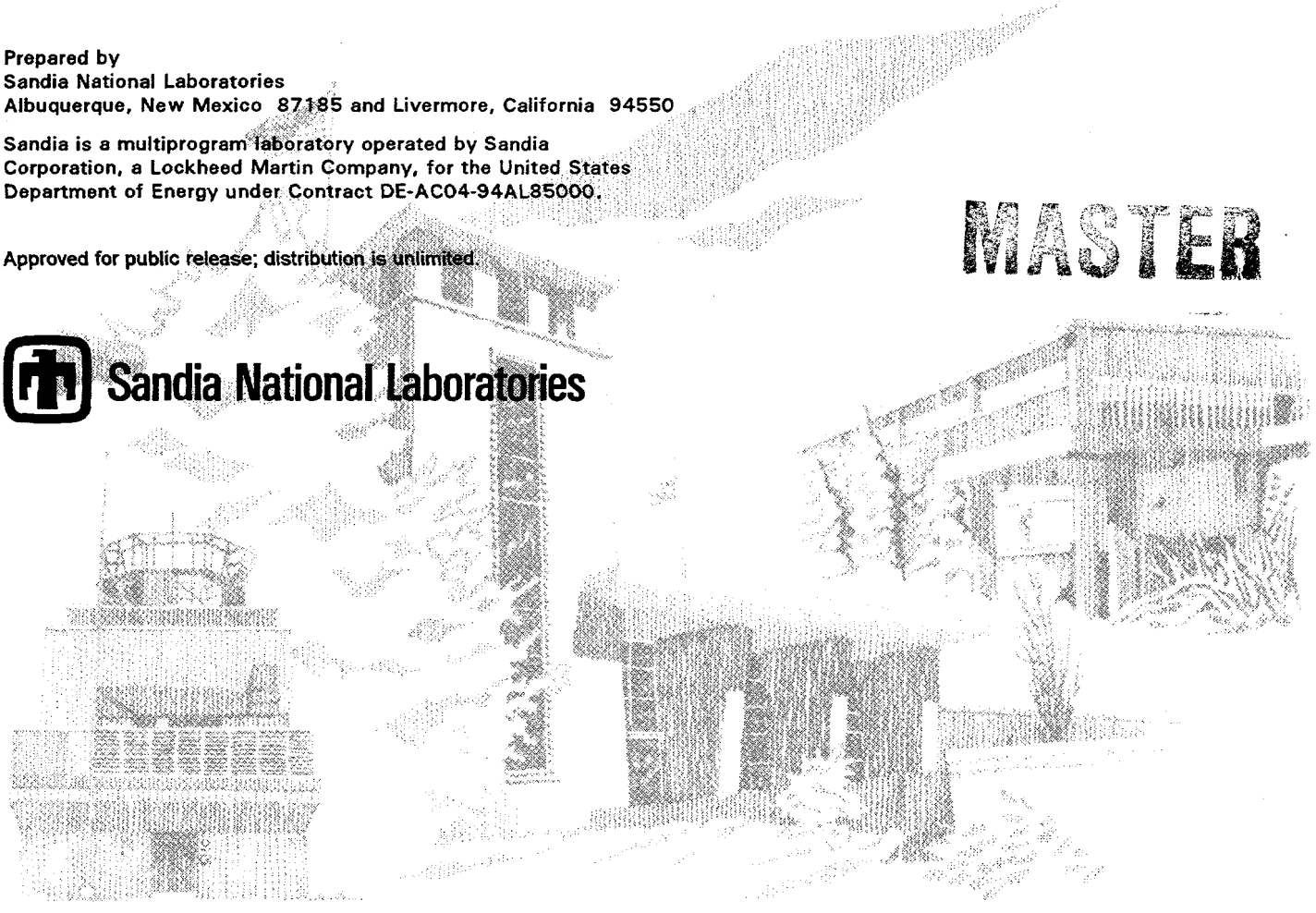

Issued by Sandia National Laboratories, operated for the United States Department of Energy by Sandia Corporation.

Available to DOE and DOE contractors from
Office of Scientific and Technical Information
P.O. Box 62
Oak Ridge, TN 37831

Prices available from (615) 576-8401, FTS 626-8401

Available to the public from
National Technical Information Service
U.S. Department of Commerce
5285 Port Royal Rd
Springfield, VA 22161

NTIS price codes
Printed copy: A03
Microfiche copy: A01

SAND97-0259
Unlimited Release
Printed May 1997

Distribution
Category UC-910

Materials and Corrosion Characterization Using the Confocal Resonator

Chris P. Tigges
Advanced Compound Semiconductor Technologies

N. Robert Sorensen
Materials Aging & Reliability:Interfaces Department

Vincent M. Hietala
Advanced Devices & Applications Department

Thomas A. Plut
Compound Semiconductor Materials & Processes

Sandia National Laboratories
P.O. Box 5800
Albuquerque, NM 87185-0603

Jon S. Martens
Wiltron, Inc.
Morgan Hill, CA 95037

Abstract

Improved characterization and process control is important to many Sandia and DOE programs related to manufacturing. Many processes/structures are currently under-characterized including thin film growth, corrosion and semiconductor structures, such as implant profiles. A sensitive tool is required that is able to provide lateral and vertical imaging of the electromagnetic properties of a sample. The confocal resonator is able to characterize the surface and near-surface impedance of materials. This device may be applied to a broad range of applications including *in situ* evaluation of thin film processes, physical defect detection/characterization, the characterization of semiconductor devices and corrosion studies. In all of these cases, the technology should work as a real-time process diagnostic or as a feedback mechanism regarding the quality of a manufacturing process. This report summarizes the development and exploration of several diagnostic applications.

Acknowledgment

The authors would like to acknowledge the considerable work occurring at the same time as this work and impacting this project both directly and indirectly. We would especially like to thank the following people: Mark S. Housel of the Advanced Devices & Applications Department and Darrel R. Frear of the Materials Aging & Reliability:Bulk Properties Department at Sandia National Laboratories, R. Withers and D. Zhang and S. Sachtjen and B. Cole at Conductus Inc., and David S. Ginley at NREL.

Contents

Figures

Tables

Summary

We have extensively studied three different classes of corrosion: corrosion of Al alloys exposed to salt spray environments, atmospheric corrosion of Cu, and Solder flux corrosion effects on electronic circuits. The Al alloy corrosion studies included the 1100, 2024, 6061, 7075 alloys of Al in ASTM standard salt spray environments. The confocal resonator successfully distinguished differences in corrosion based on the alloy type. In addition, the confocal resonator imaging capabilities detected lateral variations in corrosion which proved to be due to pit formation in the alloy samples. The confocal resonator proves to be an important new capability in this type of corrosion study. The confocal resonator was also used to characterize long term atmospheric corrosion of Cu. Inhibited Cu samples were compared with uninhibited Cu control samples. Two different inhibitors benzotriazole and imidazole were used in this study. The surface resistance at 100GHz of the set of samples was monitored periodically using the confocal resonator over an extended period of time (greater than 6 months) and a significant increase in the surface resistance was observed in the uninhibited samples while the inhibited samples of both types did not change. The confocal resonator also detected differences in surface conductivity based on the existence of flux residues at the surface as compared to clean surfaces on circuit boards. As a result, the confocal resonator is capable of evaluating cleanliness of circuit boards.

In addition to the above studies, which primarily use the measurement of surface resistance, we have also explored the use of the confocal resonator to measure dielectric properties and have applied this capability to the important outstanding problem faced by the commercial semiconductor industry namely finding an inexpensive and reliable method for characterizing high resistivity Si wafers. The confocal resonator offers several advantages in this problem including the inherent easy sample handling and nondestructive test capability. We have characterized several high resistivity Si wafer samples with respect to their dielectric properties near 100 GHz and have developed several techniques, including extensive data analysis, for reducing the results to a form directly comparable to DC transport experiments. We find that the confocal resonator can be used effectively in this application.

Nomenclature

ASTM	American Society for Testing and Materials
CR	Confocal Resonator
DC	Direct Current (used commonly to indicate any signal, not just current, at zero frequency)
GHz	Giga Hetrz = 10^9 cycles per second
HTS	High Temperature Superconducting
NDI	Non Destructive Inspection
SIMS	Secondary Ion Mass Spectroscopy
RF	Radio Frequency (used here for any high frequency signal)
2D	2 dimensional
c	speed of light in vacuum
μ	permeability
ε	permittivity
μ_0	the free space permeability ($4\pi\ 10^{-7}$ H/m)
η_0	the intrinsic impedance of free space ($\approx$377 ohms)
v_{ph}	phase velocity (nominally $Re(1/(\mu\varepsilon)^{1/2})$)
t	product thickness
Q	resonance quality factor
Q_t	measured resonance quality factor
Q_r	inverse ohmic loss
Q_c	inverse coupling loss
Q_d	inverse diffraction loss
R_s	surface resistance
R_{ss}	confocal sample surface resistance
R_{sm}	confocal mirror surface resistance
a	radius of mirror (not to be confused with radius of curvature b)
b	confocal mirror radius of curvature
d	cavity length (d=b/2 for a confocal resonator)
dp_p	spot diameter containing half of the incident power
r	confocal radial coordinate
r_s	beam radius (spot size) where the electric field is reduced by 1/e
x	confocal x-axis coordinate
y	confocal y-axis coordinate
z	confocal z-axis coordinate (sample at z = 0)
ω_0	the angular frequency at resonance
f_0	resonant frequency of the confocal cavity is approximately
Δf_0	change in resonant frequency
U_l	confocal wave energy density per unit length
Γ_s	power reflection coefficient of confocal sample
Γ_m	power reflection coefficient of confocal mirror surface
λ	the wave length of the confocal electromagnetic excitation

k	electromagnetic wave number = $2\pi/\lambda$
TEM_{xxx}	Transverse ElectroMagnetic mode xxx
p	is the integer TEM_{xxx} mode number where xxx = 00p
E	electric field
E_0	electric field at the center of the probe spot
H	magnetic field
H_0	magnetic field at the center of the probe spot
ξ	dimensionless parameter = 2z/b
φ	dimensionless parameter ratio $\tan(\varphi) = \frac{1-\xi}{1+\xi}$
K	frequency band 18-28 GHz
Q	frequency band 33-50 GHz
V	frequency band 50-75 GHz
W	frequency band 75-110 GHz

Materials and Corrosion Characterization Using the Confocal Resonator

Introduction

Surface properties are often good indicators of materials behavior in a given environment. Measurement of these properties may provide insight into interactions and changes that are occurring. A non-invasive, non-destructive technique to monitor surface properties can have application to several fields. This report documents a technique that was used to measure the complex surface impedance of conductors, semi-conductors, and insulators, and an effort to exploit that technique as a sensor. Small changes in complex permittivity in layers as thin as a few nanometers can be detected using resonant structures in the 20-100 GHz frequency range. The surface impedance extracted from the resonant data as a function of frequency in many cases allows the determination of the vertical structure of the sample with quantitative information on the thickness distribution and the complex permittivities. For many materials, this information allows reasonable chemical analysis of the sample. The use of microwave and millimeter wave frequencies as opposed to optical frequencies allows the probing of surfaces to greater depths and relaxes requirements on surface morphology. One such resonant technique, the confocal resonator, together with appropriate mathematical tools, can be used to characterize in great detail a number of different interesting surface properties.

The ability to characterize thin film processes such as atmospheric corrosion (Cu sulfidation and solder oxidation) have been investigated. Corrosion product thickness estimates determined from an analysis of the confocal resonator measurements have been correlated with mass change data from a quartz crystal micro-balance. Lateral scans of various materials have also been used to evaluate the sensitivity and resolution of this technique and to test prototype information processing algorithms. The ability to map semiconductor doping or implant profiles in 2D structures has also been investigated. We have also determined that certain well known and commonly used data analysis techniques (particularly specific digital signal processing algorithms) are inadequate when applied to data collected using the resonator technique.

Background

The Confocal Resonator

It is not the purpose of this work to explore the development of the Confocal Resonator (CR) into a diagnostic tool but rather exploring the use of the CR as a diagnostic tool for some specific applications. However, the CR as we used it was only just being commercially developed at the time of this work so the development issues are difficult to separate form utilization issues. In any event, the use of the CR has been difficult for instrumental as well as reasons inherent to CRs. The data that we gathered using the laboratory prototype CR proved to be extremely rich and are beyond the present level of simple theory regarding CRs. This richness, can in principle, be exploited in the future but until now has actually made it difficult to use the CR in practice. Appendix A describes the CR in greater detail than required to understand the material that follows and has been included here for completeness and because the details are important in

inferring material properties from actual CR measurements. Refer to Figure 13 in Appendix A for a schematic representation of the apparatus used in this work.

The CR is an open resonant structure[1] with two "reflectors" (the spherical mirror and the planar sample under test). The mirrors are generally made out of aluminum although if sensitivity improvements are needed, silver or gold coatings are possible as are fully superconducting mirrors. The mirrors are typically 8-10 cm in diameter with radii of curvature ranging from 5-15 cm depending on the frequency range and field distributions required. The mirror focuses the fields onto the planar sample increasing the sensitivity to material changes on the sample.

CR measurements directly produce two important quantities: the quality factor Q and the resonant frequency f_0. In this work, the frequency range is determined by the mirror geometry (K, Q-V, and W band mirrors were used) and the mode used within each band. However, the most commonly used range in this work is 90–100 GHz. The resonant frequency can be placed anywhere in the mm-wave range by proper choice of cavity geometry. The specific frequency range chosen is a compromise between high lateral resolution made possible by operating at higher frequencies and the economics which at this time favors operation at lower frequencies . The quality factor is inversely related to the line width of the resonance and is determined by the losses within the cavity. There are several sources for cavity loss but in typical applications the sample losses composed of resistive or dielectric loss dominate. For conductive samples, the surface resistance can be extracted from a simple formula [2]

$$R_{ss} = \frac{\pi f_0 \mu_0 b}{2Q} - R_{sm} \qquad (1)$$

where b is the radius of curvature of the mirror, μ_0 is the free space permeability ($4\pi\ 10^{-7}$ H/m) and R_{sm} is the sperical mirror surface resistance in ohms. The surface resistance, R_{ss}, is the variable used in many of the plots to follow and is a good measure of the overall loss in a composite sample. The surface resistance represents the difficulty in inducing RF currents on the surface of the sample. Any semiconducting or insulating corrosion products or cracks formed on the surface will radically affect the ability to generate these currents and will result in an increased surface resistance.

In many cases, it is of interest to relate the materials parameters of a coating (permittivity and permeability) to the surface impedance that would be measured. A simple two layer model will be assumed (a coating or product on a conductor). As discussed above, the resonant frequency shifts because of the presence of a layer of different wave velocity. Thus, the difference in resonant frequency (with and without the product layer) provides information on the layer's properties and thickness. This relation is expressed as [3]

$$t \propto \frac{\Delta f_0}{c/v_{ph} - 1}$$

where t is the product thickness, Δf_0 is the change in resonant frequency and v_{ph} is the phase velocity in the material (nominally $\mathrm{Re}(1/(\mu\varepsilon)^{1/2})$). This effect will be dominated by the real parts of permittivity and permeability under lower loss conditions. More generally, the complex composite surface impedance (composite since it includes the effect of the coating and the underlying conductor) can be expressed as[4,5]

$$Z_{s,comp} = \sqrt{\frac{\mu}{\varepsilon}} \frac{R_{s1}(1+j) + \sqrt{\frac{\mu}{\varepsilon}} \tanh\left(d\sqrt{-\omega^2 \mu\varepsilon}\right)}{\sqrt{\frac{\mu}{\varepsilon}} + R_{s1}(1+j)\tanh\left(d\sqrt{-\omega^2 \mu\varepsilon}\right)}$$

where R_{s1} is the surface resistance of the underlying conductor (normally a few hundred milliohms at 94 GHz for most metals), d is the coating thickness, and μ and ε are the complex permeability and permittivity of the coating/product (respectively). The imaginary part of $Z_{s,comp}$ is manifested in the measured resonant frequency, since changes here represent changes in the phase length of the cavity. The real part of $Z_{s,comp}$ is the composite surface resistance and is derived from the directly measured cavity Q. There are two things making this expression frequency dependent. The coating/product acts as a transformer in many cases so there will be some frequency dependence (in the tanh function) from changing electrical thickness of the coating. The material parameters μ and ε may also be frequency dependent. In most corrosion products studied to date, the material frequency dependence has been a relatively minor effect.

Analysis

In the analysis of samples, the surface resistance and resonant frequency are normally measured as a function of position. The complex dielectric parameters can then be extracted as a function of position. The absolute values can give information about the corrosion products since they represent deviations from the base metal. Loss tangent is often useful in assessing the purity of a corrosion product film (aluminum oxide on Al, for example) while the real part of permittivity can often give more compositional information (separating CuS from Cu_2S as an example). The variation of these properties with position can be interesting in itself. Variations in corrosion product properties can give some insight into nucleation events and substantial deviations in surface resistance can be used to locate corrosion-induced defects. The examples in the rest of this document illustrate how the extraction of these properties can be used to investigate, among other things, the corrosion reactions observed on a variety of materials and structures.

As shown in Figure 13, the mirror is isolated from the sample. This allows *in situ* diagnostics by focusing the beam through a thin window (about 6 mil quartz or mylar among other choices). There are few constraints on the sample size: it must be greater than a few mm in each lateral dimension although larger dimensions help for sensitivity. Historically, these structures have been used for evaluating the properties of dielectrics[6] or conductors and superconductors[2]. The shape and frequency of the resonance provide information on the complex permittivity of the materials in the beam path as discussed else where.[4,7] As long as all of the objects in the beam path are electrically small (except for a final back conducting plane), information extraction is relatively easy including the vertical distribution of complex permittivity. This latter process relies on the measurement of the surface impedance as a function of frequency. For a material dominated by normal electron conduction, the $1/e$ penetration distance of the field into the material is given by

$$\delta_s = \sqrt{\frac{1}{\pi f \mu_0 < \sigma >}} \tag{2}$$

where f is the measurement frequency, μ_0 is the free space permeability (non-magnetic materials are assumed for now) and $<\sigma>$ is the local average of conductivity. The point is that the probing region of the field changes with frequency in a predictable way. From the variation of surface impedance with frequency, the changes in complex permittivity (generally equivalent to a knowledge of complex conductivity) can be extracted by deconvolution. The relationship between the material parameter $\varepsilon(z,\omega)$ and the measured surface impedance is actually fairly complicated:

$$Z_s(\omega) = \frac{1 - \frac{1}{2}\int_0^L \left\{ e^{-2\int_0^z \gamma(x)dx} \frac{d}{dz}[\ln(\overline{\eta})] \right\} dz}{1 + \frac{1}{2}\int_0^L \left\{ e^{-2\int_0^z \gamma(x)dx} \frac{d}{dz}[\ln(\overline{\eta})] \right\} dz} \tag{3}$$

where η^p and γ^q are rational functions of $\varepsilon(z,\omega)$ and frequency (p and q are small integers) and L is some distance into the material after which there are no significant material changes. In the actual solution process, this equation is numerically inverted, with some assumptions about the structure of the sample, to decipher the vertical structure of the sample under test.

Results

Atmospheric Corrosion of Cu

In the case of Cu metal sulfidation, we have been able to utilize the atmospheric corrosion facility to demonstrate both *in situ* and *ex situ* measurement capabilities of the confocal resonator. The *in situ* measurements were configured so that H_2S gas flowed directly over the surface of a sample being measured. A mylar film window was used to contain the corrosive gas while allowing continuous measurement of the surface electrical properties associated with copper sulfide film growth. These measurements have also been compared with interrupted *ex situ* measurements where the sulfidation occurred in a well controlled environmental chamber and the samples were removed for CR analysis. The sulfide corrosion product films were determined to involve two film layers: a Cu_2S layer at the metal-film interface and a CuS outer layer. These layers can be resolved by the confocal resonator due to differences in micro-wave impedance characteristics.

Figure 1 is a schematic of the *in-situ* experimental setup. In this case, two Cu samples were exposed to the corrosive gas: a bulk Cu sheet for CR and a sputter deposited film of Cu on a quartz crystal for mass change measurements. The bulk Cu sample is housed in a cell with a 150 μm mylar window through which the confocal resonator could measure the sample. The calculated film thickness (found to be mainly CuS at early growth stages) from the confocal and quartz crystal measurements are

shown in Figure 2. The measurement was continued in a slightly different atmosphere for much longer exposures. It was found that the composition of the growth layer began changing from Cu_2S to CuS as it thickened (several tens of nanometers) as shown in Figure 3. The CR data are compared with mass change data, with an upper bound assuming Cu_2S and a lower bound assuming CuS. It is again clear from these data that the sulfide film is predominantly Cu_2S at short times and CuS at longer times. The thickness information is derived from the $Z_s(\omega)$ measured data while assuming a simple 2 layer model for the sample (Cu with some dielectric-like growth on top). This illustrates the ability of the technique to separate stoichiometries of various growth regimes while allowing accurate thickness determination.

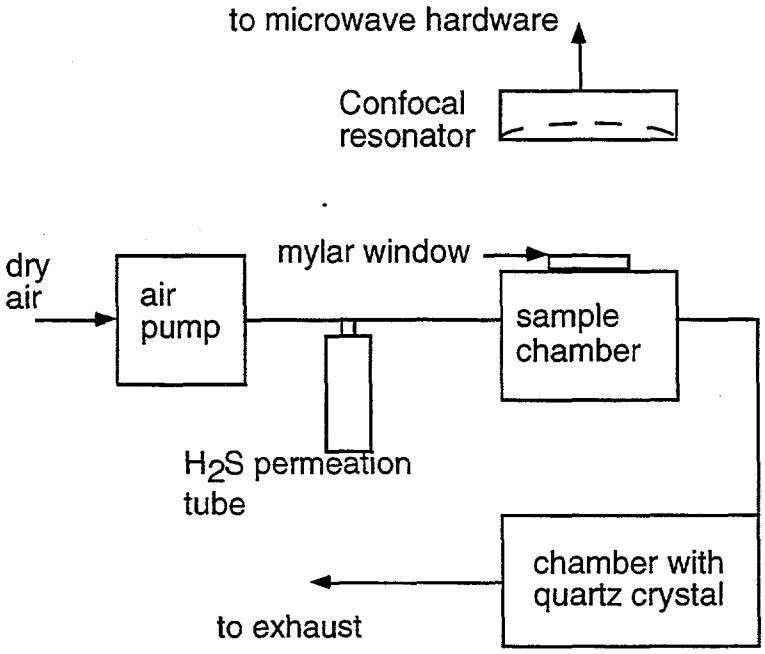

Figure 1. Experimental arrangement for an *in situ* sulfidation experiment. The sample and a quartz crystal microbalance are exposed to the same H_2S-air gas stream. The surface resistance of the sample is measured with the use of a mylar window on the test cell

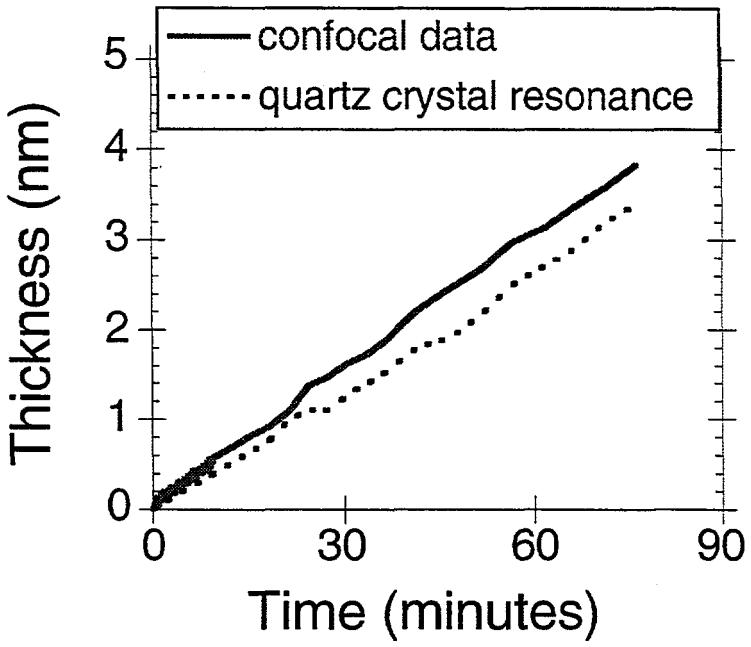

Figure 2. Thickness of a sulfide growth layer on copper as a function of time from both quartz crystal and confocal data.

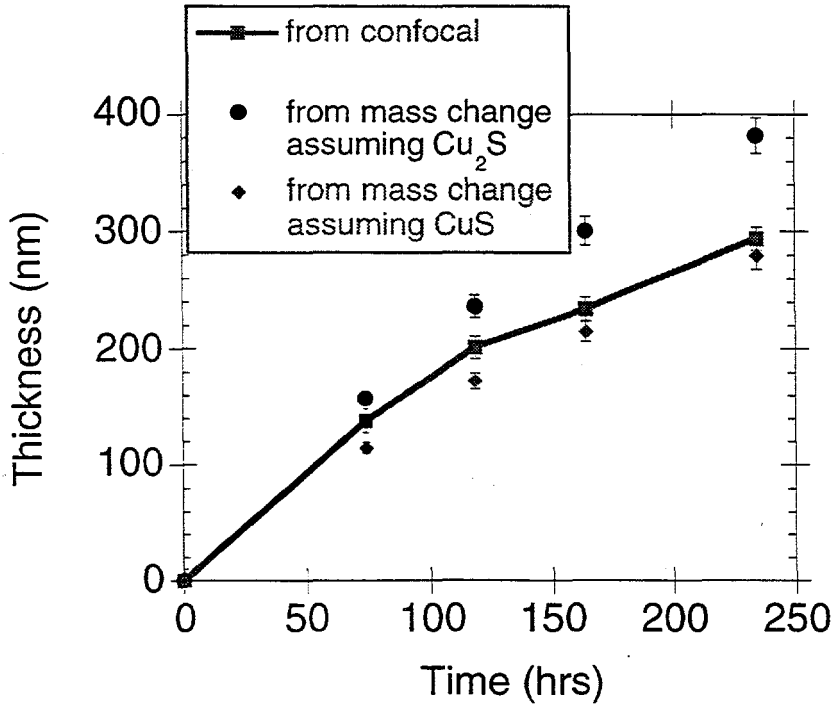

Figure 3. Thickness growth of the copper sulfidation experiment over a longer period of time (confocal calculated and that from mass change data).

The confocal resonator was also used to characterize long term atmospheric corrosion of Cu. Inhibited Cu samples were compared with uninhibited Cu control samples. Two different inhibitors benzotriazole and imidazole were used in this study. The surface resistance at 100GHz of the set of samples was monitored periodically using the confocal resonator over an extended period of time (greater than 6 months) and a significant increase in the surface resistance was observed in the uninhibited samples while the inhibited samples of both types did not change.

Solder Flux Residue Detection

The confocal resonator also detected differences in surface conductivity based on the existence of flux residues at the surface as compared to clean surfaces on circuit boards. As a result, the confocal resonator is capable of evaluating cleanliness of circuit boards.

PbSn Solder Oxidation

Solder oxidation is believed to play a role in thermo-mechanical fatigue of solder joints. It is suspected that both water vapor and oxygen play a role in the solder oxidation process, producing a surface tin oxide. As with the copper sulfidation process, two oxidation states of Sn are possible (Sn^{+} and Sn^{+2}). In this example, bulk PbSn solder samples were a variety of environments. In one case, the sample was exposed to a 70 °C 90% relative humidity atmosphere for a period of time and periodically the surface impedance was determined as a function of frequency. While not *in situ*, this is a preliminary experiment to look at solder behavior (a closed test cell is under construction for later experiments). The real part of the permittivity is shown in Figure 4 as a function of time and suggests the early formation of SnO followed by the later growth of the more stable SnO_2. The thickness of the growth calculated from this technique is similar to that calculated with other techniques. A calculated profile of permittivity (after the experiment) as a function of depth is shown in Figure 5. These data, determined from the frequency dependence of the surface impedance, again suggests an early growth of SnO followed by growth of SnO_2.

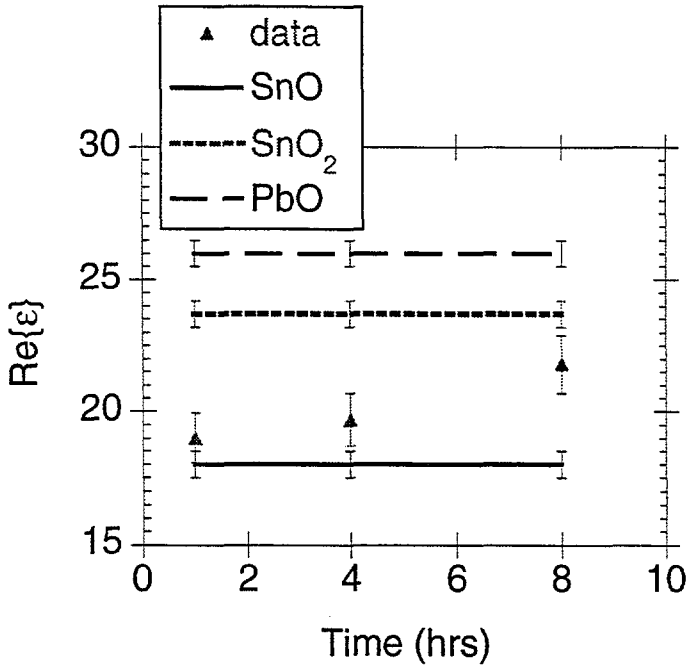

Figure 4. Permittivity of oxide growth layer on PbSn solder as a function of time as well as the values for several stoichiometries. A SnO layer appears to grow initially followed by a SnO_2 layer.

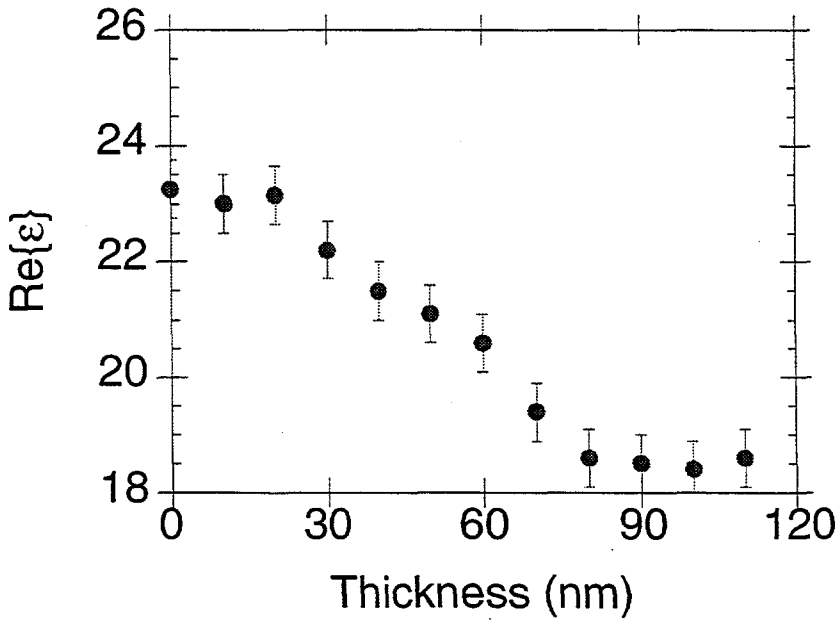

Figure 5. Calculated profile of the real part of permittivity of an oxidized PbSn solder sample. The data suggests an early formation of SnO followed by the formation of SnO_2.

In a second experiment, several PbSn solder samples were prepared by controlled exposure to N_2(as a control), O_2 and air/water vapor. These were then analyzed using confocal resonator techniques. Table 1 present data on the solder oxidation. The column F (SnO thickness) is very approximate little since it is hard to define when the transition begins. Two layers of tin oxide are formed during exposure. The inner layer is a very thin SnO layer that is generally less than 10 nm thick and forms at the solder surface. This layer grows roughly linearly but weakly with exposure time and depends significantly upon the exposure environment as can be seen by the results shown in Figure 6. Both the growth rate and final thickness of the SnO layer are a function of environment, with the wet environment producing the thickest layer. A second layer forms above the first, interfacial, SnO layer and its growth kinetics are quite different. In nitrogen, there is very little film growth. In the O_2 environment, the oxide growth exhibited linear kinetics over the exposure time, with an eventual film thickness of around 50 nm (Figure 7(a)). The film did not reach a limiting thickness or transition into diffusion controlled kinetics. In contrast, the samples exposed to water vapor exhibited similar kinetics initially, but appeared to transition into a diffusion controlled region with longer exposure times. The SnO film thickness was not dramatically affected by the environment, but the SnO_2 film was roughly twice as thick in the water vapor environment as in the oxygen experiment (Figure 7(b)). This result may indicate that, in the water vapor case, the kinetics are either O_2 or Sn diffusion limited.

Table 1. Data on the solder oxidation.

A: sample number
B: environment
C: hours of exposure
D: hours at 125C/-55C
E. total oxide thickness (nm)
F: estimated SnO thickness near interface (nm)

A	B	C	D	E	F
1	N2	18.8	3.13	05.2	2.1
2	N2	41.5	6.90	05.2	2
3	N2	50.0	8.30	05.9	2.3
4	N2	72.5	12.1	05.6	2.1
5	O2	18.2	3.04	20.0	3.8
6					
7	O2	26.0	4.30	25.6	4
8	O2	48.0	8.00	41.3	4.5
9	(60% H20 v)	19.5	3.25	62.9	6.8
10	(60% H20 v)	47.5	7.90	102.9	7.5
11	(60% H20 v)	47.5	7.90	98.0	7.8
12	(60% H20 v)	72.0	12.0	107	8.9
13	O2	36.0	6.00	33.3	4.3

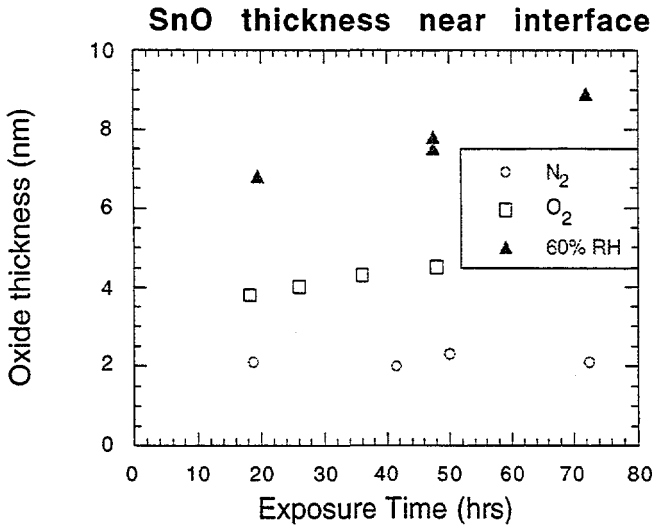

Figure 6. The growth as determined by the confocal resonator of the thin SnO interfacial layer with exposure time in various environments.

Aluminum Alloy Salt Spray Corrosion

The Al alloy corrosion studies included 1100 (commercially pure), 2024 (Al, Cu, Mg), 6061(Al, Mg, Si), 7075(Al, Cu, Mg, Zn) alloys of Al in ASTM standard salt spray environments. The confocal resonator successfully distinguished differences in corrosion based on the alloy type. In addition, the confocal resonator imaging capabilities detected lateral variations in surface properties which proved to be due to pit initiation in the alloy samples. All 4 aluminum samples were measured before and after salt fog exposure (168 hours, 5% solution of NaCl in water atomized, 95°F). The object was to correlate the surface impedance/permittivity signatures extracted from the resonant technique with microscopic analysis.

Before exposure, the surface resistances of the alloys were all reasonably consistent with what one would expect for these bulk metals with an air formed oxide. Starting samples with varying levels of oxides affected the absolute numbers but not the relative changes to any great degree. After exposure, the surface impedance changed dramatically as indicated in Table 2. Here W=windward and L=leeward refers to the side of the sample receiving and looking away from the salt fog generator respectively. The measured numbers are surface resistances in ohms.

Table 2. Al alloy salt spray results.

Alloy	Before	After W	% change	After L	% change
1100	0.176	0.226	*+28%*	0.208	*+18%*
6061	0.222	0.305	*+37%*	0.266	*+20%*
7075	0.258	0.461	*+79%*	0.376	*+46%*

There is clearly a difference among the alloys in corrosion resistance, as has been confirmed by many other measurement techniques (quartz microbalance, microscopic

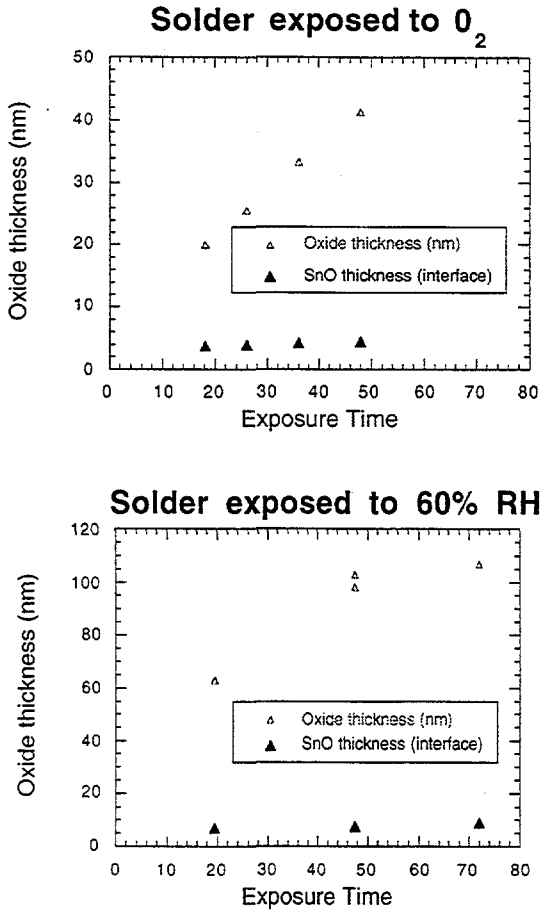

Figure 7. Oxide thickness determinations form confocal resonator measurements: (a) the relatively fast linear growth of a SnO_2 layer above the SnO interfacial layer with O_2 exposure time. (b) the decreasing rate of growth of the SnO_2 layer with water vapor exposure time.

inspection, electrochemical tests. ...). The thickness of the corrosion products was extracted from resonant frequency differentials and the ratio of these thicknesses (1100 product thickness:6061 product thickness: 7075 product thickness) was about 1:2.2:4. Compared to an overage thickness assessment from profilometry, the extracted thicknesses were accurate to within about 5%. This is not necessarily a meaningful comparison since the thickness variations across the samples were substantial. The permittivities were reasonably stable (5% shifts) suggesting the bulk of the differences in surface resistance signature are due to impurity incorporation. Before and after contour maps of the 6061 alloy are shown in Figure 8 to illustrate the fairly dramatic nature of the surface resistance shift.

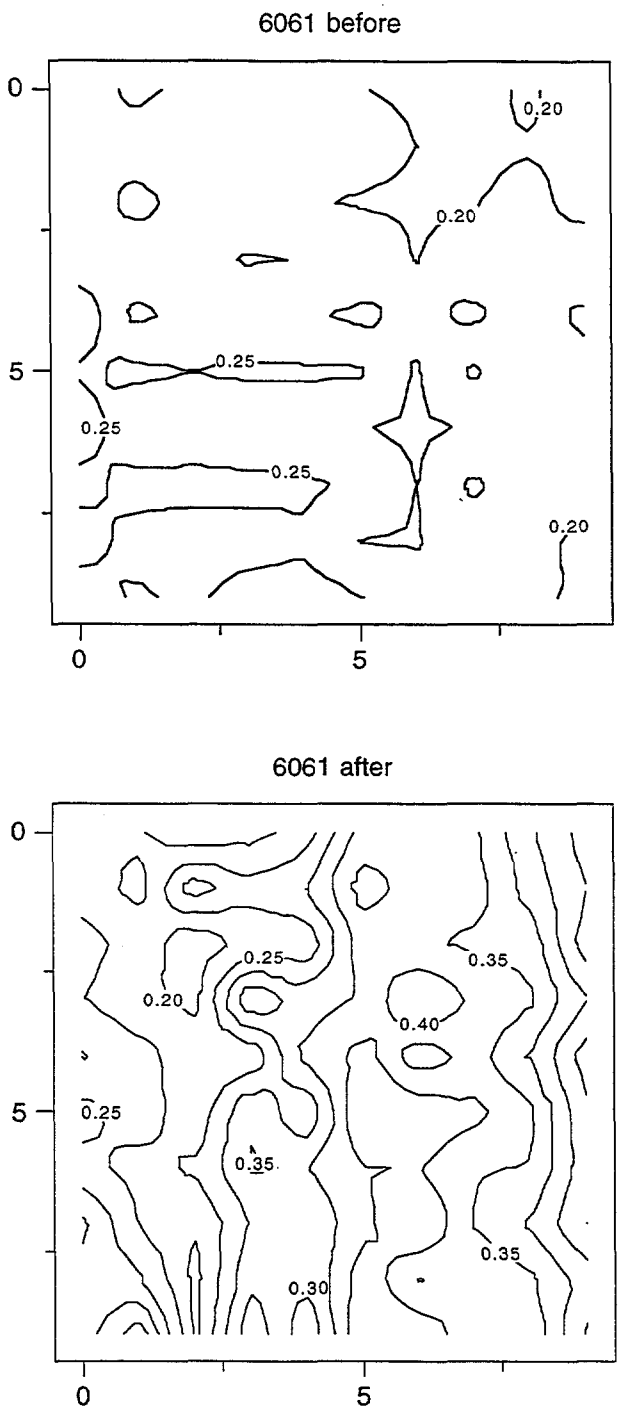

Figure 8. Contour plots of a 6061 Al section before and after salt fog exposure. The contour labels are surface resistances in ohms. The absolute change is obvious as is the increase in inhomogeneity due to pitting corrosion. Lateral scales are 2 mm/div (full scale, the plots are 10 divisions wide).

The loss tangent of the product layer also increases through the series of samples from about 0.005 to 0.015. The accuracy on the loss tangent extraction is again about 5% in this range but repeatable to within about 1%. Since the loss tangents are all higher than that of pure Al_2O_3, the product layers are becoming increasingly diverse chemically as one moves through the series with the 7075 product layer being dominated by contaminant oxides. This is also consistent with many microscopic observations. Also of interest is that the standard deviation of loss tangent (on a spatial basis) is about 8 times higher for the 7075 than for the 1100 suggesting a 7075 nucleation model with very different distance scales.

These observations would be consistent with nucleation centering on the denser impurity sites. Further evidence is provided by some limited multi-frequency analysis which showed the standard deviation of loss tangent decreasing away from the metal surface. The complex dielectric properties would be more unstable near these impurity sites and would presumably become somewhat more stable at the upper layers of the product.

Al 7075 Alloy Sample with Rivet Holes and other Stresses

Since a critical corrosion problem for aircraft structures involves subsurface cracking near rivet holes, samples were generated to simulate this condition . Rivet holes were placed in a 7075 coupon (1/8" thick) that had already had salt fog exposure but was not coated with any pretreatment. The sample was then placed under bending stress while in a salt water environment (to accelerate any effects) for 24 hours. The before and after contour maps are shown in Figure 9. Prior to the stress and exposure, the holes were clearly defined by deviations in local surface resistance. After exposure, another region of elevated surface resistance appeared around the hole areas that is asymmetric. Since the bending force was applied against the vertical edges of the image, this may be consistent with microcrack formation. A more complete analysis needs to be done of this type of test, but a change was detected around the holes that could not be detected optically.

Some additional tests were conducted to try to correlate the surface resistance signature with the exposure conditions and, if possible, to the incipient crack sizes. A measure that was used was the effective area that had a surface resistance elevated at least 50% above the background mean. Since the rivet hole sizes were constant (diameter of about 5 mm), this should provide a measure of the disrupted area. Because of time constraints, only a limited number of tests were run, but the data illustrates a clear trend (see Table 3). Keep in mind that the effective area includes the rivet hole itself. Small cracks were microscopically evident for the last row in the table with sizes on the order of 100 μm. This should give some estimate of the measurable effect size.

Table 3. Effective elevated damage area under stressed salt exposure.

Conditions	Effective elevated area (mm^2)
1 day, nominal bending stress	76
2 days, nominal bending stress	81
3 days nominal bending stress	85
4 days, double bending stress	93

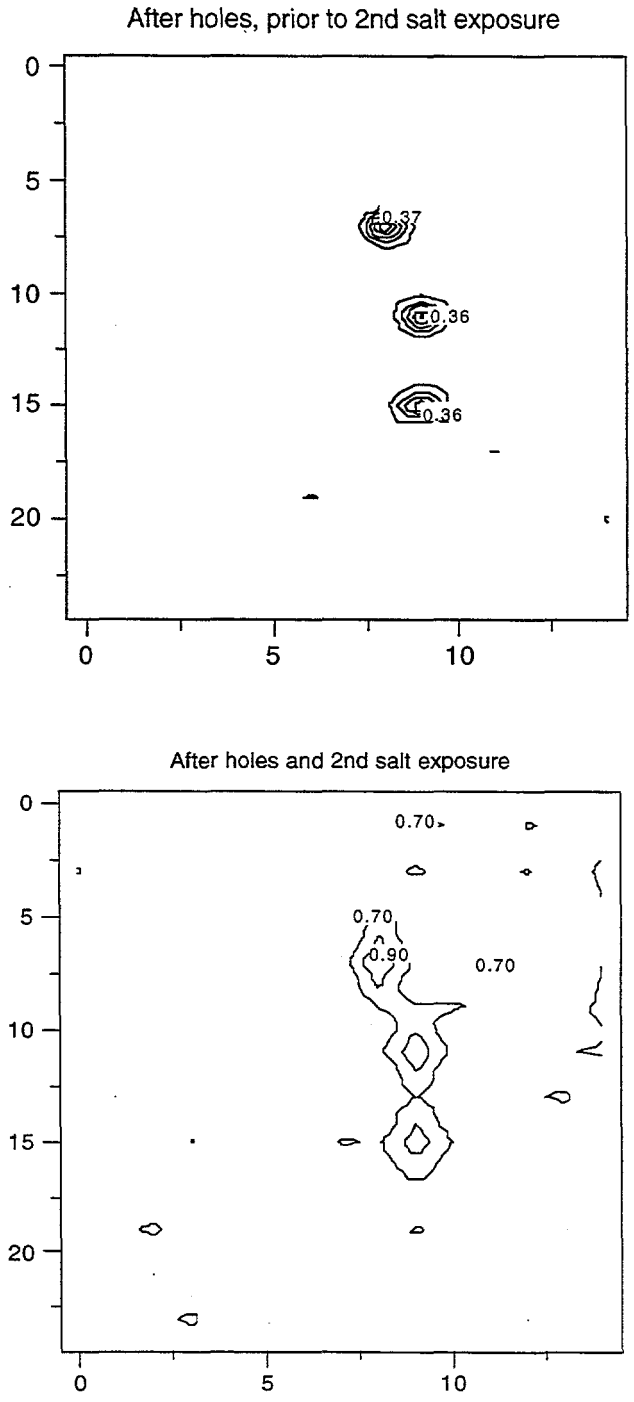

Figure 9. Surface resistance plots of 7075 coupon with rivet-like holes. The images are before and after salt exposure. Note the added elongated distortion in the surface resistance data after exposure. The contour values start at a high level to focus on the hole areas. The significant surface disruption of the corrosion on the blank metal is not shown.

Salt Exposure Underneath Paint

Since in many field applications it is desirable to detect corrosion beneath paint, it is important to determine if (a) paints are too lossy to allow this measurement and (b)what degree of sensitivity is possible. The first experiments were conducted with steel coupons painted with either epoxy or powder paints. A scratch of 1±0.2 mm width was cut in the paint and the coupons exposed to salt fog. The final coupon was then measured to see if corrosion was detectable beneath the paint. Figure 10 shows the results for two coupons measured under these circumstances. The scratch extends horizontally from x=0 index marks to about x=10 in both cases. The background surface resistance stayed in the 0.3-0.4 ohm range but the disruption near the scratch is significant. In the heavy exposure case, disruption in surface resistance is visible nearly 2 cm from the scratch. Since the spot size is certainly no larger than 5 mm, this indicates the presence of products beneath the paint surface at a significant distance from the scratch. The total disruption width is about 50 mm in the heavy case and 35 mm in the moderate case.

The experiments were repeated on some aluminum samples and in no case was the paint loss a significant factor in corrosion detection. The disruption on surface resistance did not exceed 7% while the relative change in the corroded areas was easily 20-40% and sometimes orders of magnitude as shown in Figure 10. The paint clearly impedes extraction of the real part of permittivity since an additional phase delay source is present but it should be less of a problem in detectability. This ability is extremely important in field application, since bare surfaces will often not be available.

Titanium in a Heated Saline Environment

An alloyed Ti sample was exposed to a heated saline environment as an initial test. While this test clearly does not mimic the actual environment an engine part would be subjected to, it can help establish a detectability limit for the analysis. The primary growth will probably be a contaminated oxide, which should be detectable as in the aluminum alloys, but layer growth may be slower. Before and after exposure contour maps are shown in Figure 11.

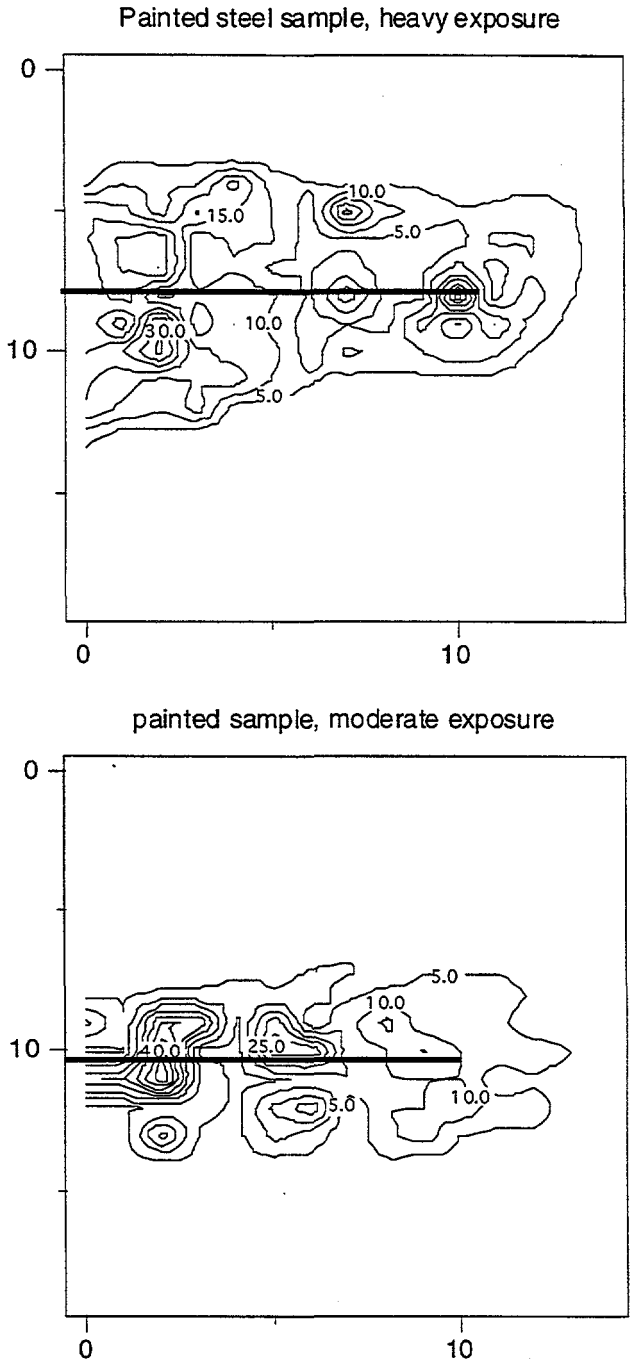

Figure 10. Contour plots of a painted steel sample scratched and exposed to salt fog. Contour plots are of a 1 mm wide scratch and two different salt fog exposure durations. The lateral scales are 5 mm/div and the contour labels are surface resistances. The position of the scratch is indicated approximately by the heavy black line.

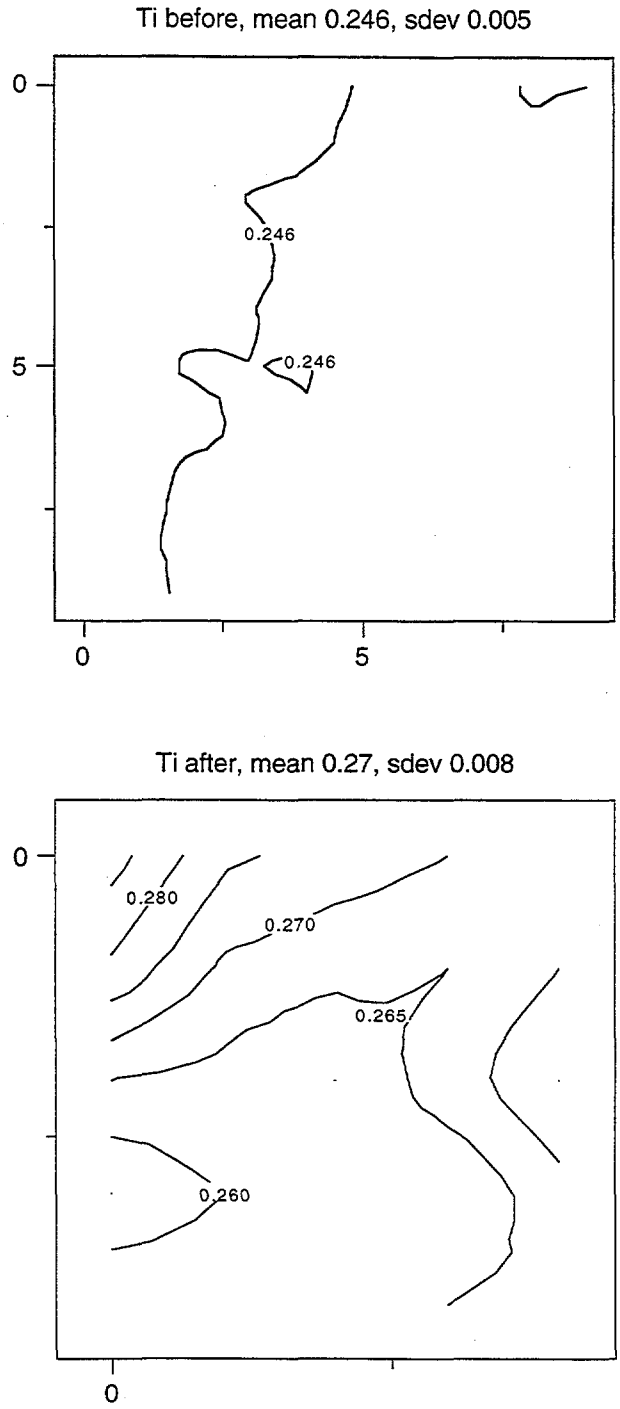

Figure 11. Ti sample exposed to heated saline. Plots before and after heated saline exposure. While more subtle than some of the other samples, the change in surface resistance is distinct and statistically significant.

While more subtle, the changes here were detectable and were not visible with the unaided eye. The dielectric constant on the product material was approximately 20.5 with an uncertainty of about 5%. Since this is far below the value for TiO_2, it is likely the product is dominated by sub oxides or oxides with the impurities in the alloy. With additional experimentation, a better estimate of the composition of the oxide could be retrieved. The main purpose of this experiment was to confirm detectability in another important materials family.

High Temperature Superconducting Material Exposed to 0.1% HNO_3 Solution

Of increasing importance in the development of superconducting integrated circuits is the degradation incurred during the processing of these sensitive materials. As an example, weak acids are often used as etches but have been known to cause significant damage to exposed surface of the high temperature superconducting (HTS) material. While this apparently is not a practical issue since the desired planar surfaces are not exposed to the etchant, the edges of transmission lines are. For many planar transmission lines, this is the region of highest current density hence edge degradation is very important. To evaluate this, a wafer of the superconductor YBaCuO was measured before testing and then exposed to a 0.1% HNO_3 solution for approximately 1 s. The vertical profile is shown in Figure 12 (in terms of the real part of permittivity) and suggests the reduction of material (as expected) coupled with the formation of a surface layer. The poor conducting nature of this level is consistent with observed circuit degradation and with the formation of a $BaCO_3$ layer that was theoretically expected.

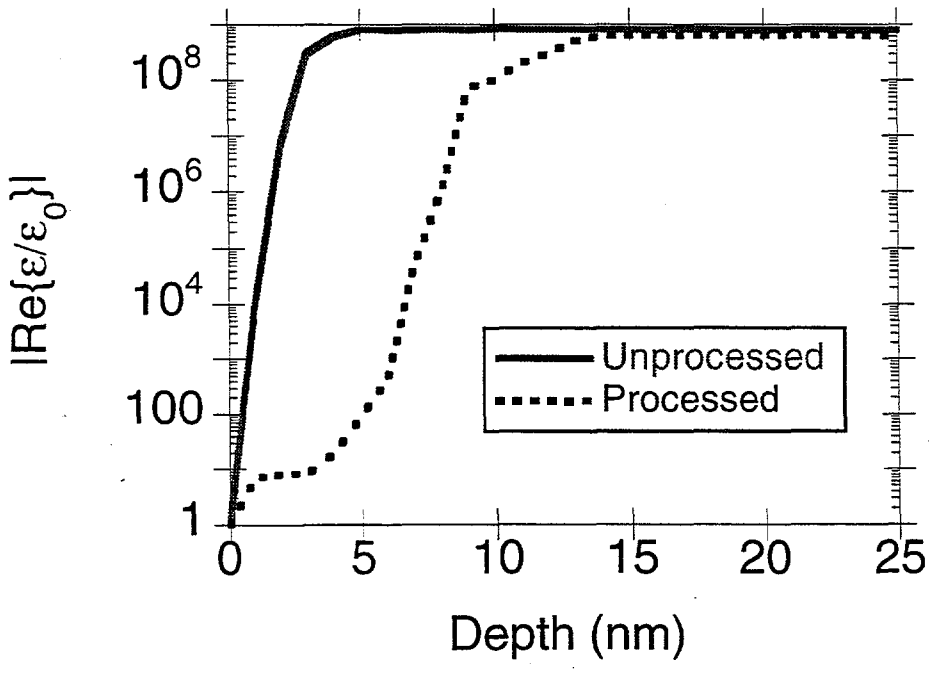

Figure 12. Vertical profile of the normalized real part of the permittivity of a YBaCuO superconducting wafer before and after exposure to an HNO_3 solution. A surface quasi-insulator appears whose properties are consistent with $BaCO_3$.

Dielectric Properties

In addition to the above studies, which primarily use the measurement of surface resistance, we have also explored the use of the confocal resonator to measure dielectric properties and have applied this capability to the important outstanding problem faced by the commercial semiconductor industry namely finding an inexpensive and reliable characterization of high resistivity Si wafers. The confocal resonator offers several advantages in this problem including the inherent easy sample handling and nondestructive test capability. We have characterized several high resistivity Si wafer samples with respect to their dielectric properties near 100GHz and have developed several techniques, including extensive data analysis, for reducing the results to a form directly comparable to DC transport experiments.

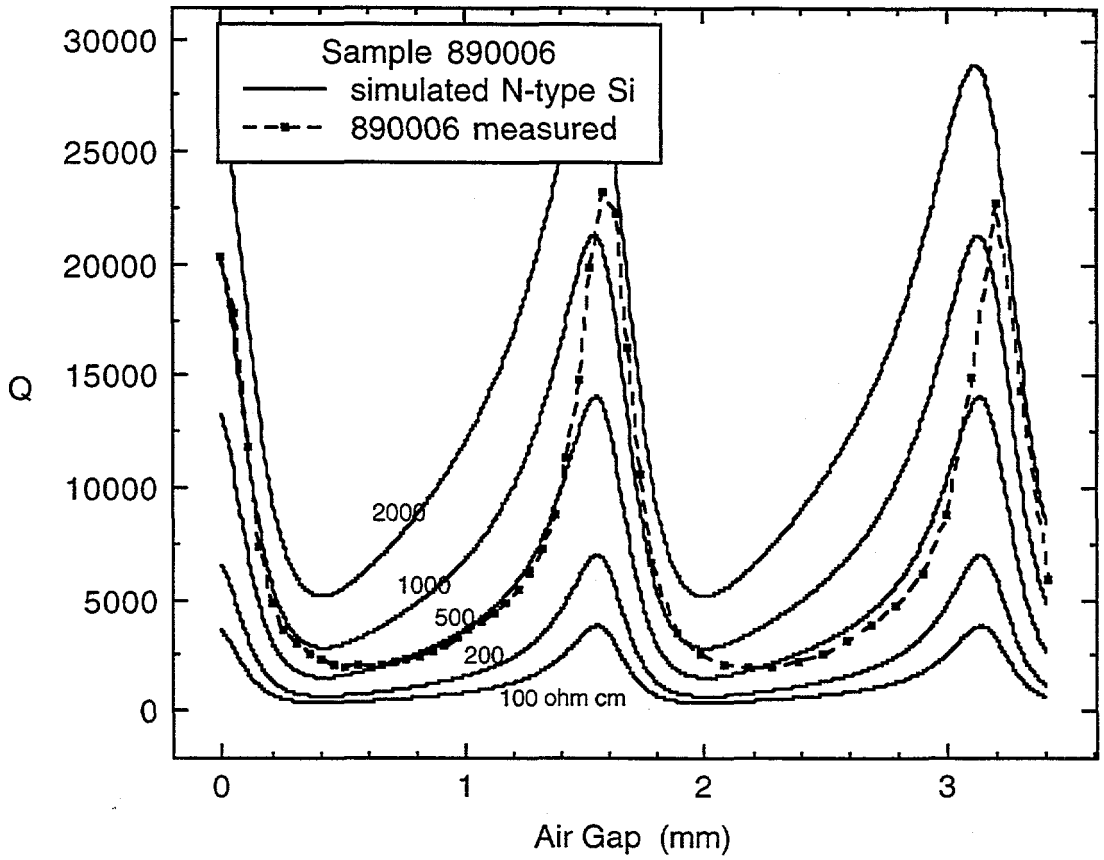

Figure 13. The air gap dependence of the measured and simulated Q of an N-type Si sample. A known air gap is introduced between the sample and a thick metallic substrate. Several simulations differing in dopant concentration (resistivities) are shown for comparison. Note the steepness of the dependence near zero gap thickness.

In most of these measurements a thin (~1mm thick) dielectric sample is placed over a thick metallic substrate. The substrate surface resistance and sample thickness are usually, but not necessarily, considered to be known quantities and are determined by independent measurements. Measurements of dielectric properties using this set up require some care since the results can be quite sensitive to the vertical position of the

sample in the cavity (see for example Figure 13). In particular, the Q and or f_0 can be altered considerably by the inadvertent introduction of a small air gap between the dielectric sample and metallic substrate (see Figures 13 and 14). It is practically inevitable that some air gap exists as a result of a nonideal shape or of cleanliness of either the sample or the substrate. As a result, it is prudent to take a series of measurements intentionally varying the air gap thickness by known amounts and comparing the measurements with numerical simulations to infer the sample properties. We have developed several computer models to facilitate this type of analysis and have applied them in analyzing the measurement results gathered on several high resistivity Si wafer samples. The models generally take as input or otherwise infer relevant properties of the dielectric material and the cavity geometry used during a study. Sample properties such as thickness, permeability, permittivity, conductivity effective mass, transport relaxation time, and carrier concentration are considered in the present application. These properties are not necessarily intrinsic but are established by the physical based model used to simulate the electromagnetic material properties as they apply to the CR measurement. As can be seen in Figures 13 and 14, the correspondence with f_0 is quite good while the present models appear to be inadequate for Q and give only a qualitative correspondence at this time. We are confident that more sophisticated modeling can be applied to resolve the outstanding disparity between the measurements and the simulations.

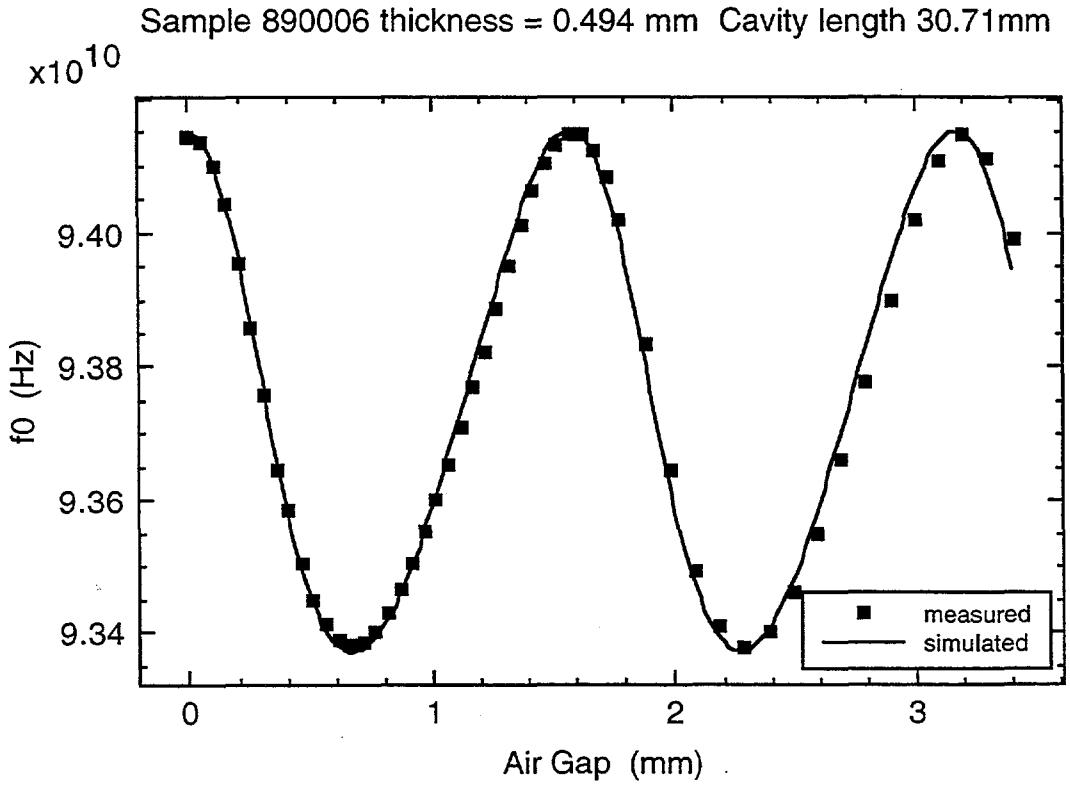

Figure 14. The air gap dependence of the measured and simulated f_0 of an N-type Si sample. Note that f_0 is not as sensitive as Q in this case to deviations from zero gap thickness.

As can be seen Figure 15, below about 1 (ohm cm), Q is not air gap sensitive and approaches the metallic substrate limited value as the sample resistivity approaches zero. Above 1 (ohm cm), Q is quite sensitive to the air gap thickness. The sensitivity of this method is limited to resistivities less than about 10^5 (ohm cm) as an air gap dependent asymptote results above this resistivity level. It should be noted that, although Q is not a single valued function of resistivity, the air gap thickness dependence changes at 1 about (ohm cm) and the correct resistivity can be easily inferred from this dependence except near 1 (ohm cm).

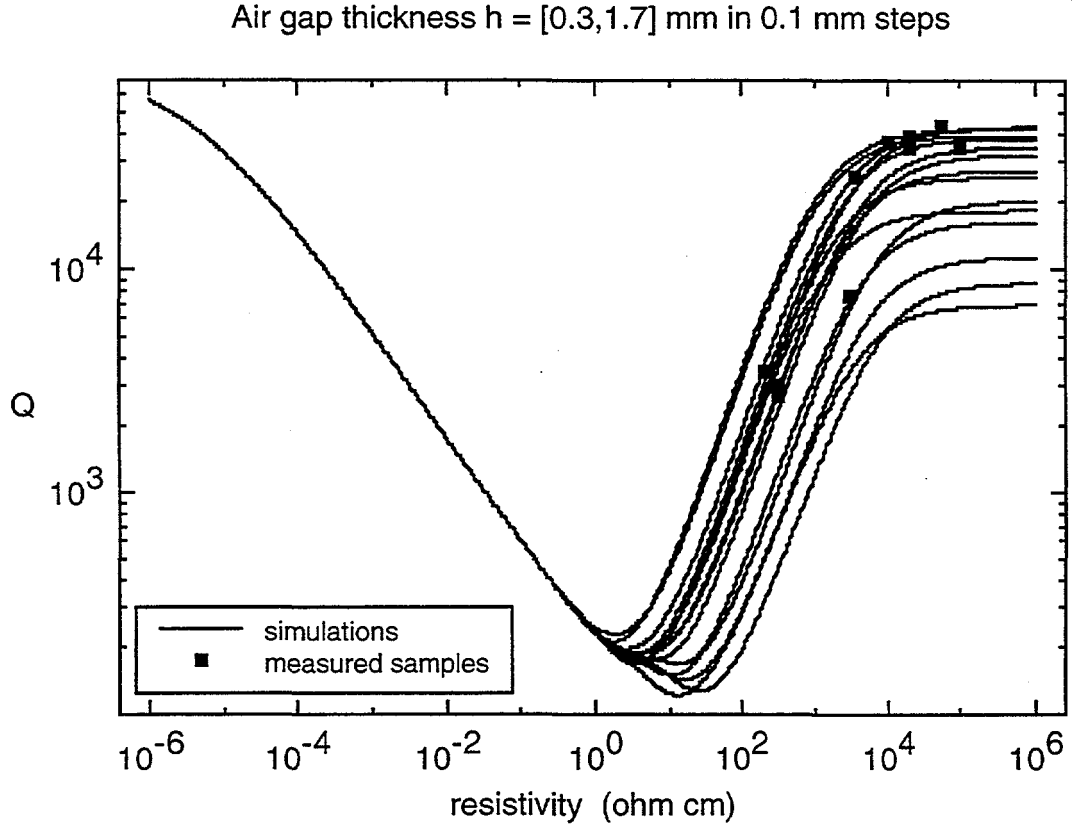

Figure 15. Simulated and measured resistivity dependence of Q for N-type Si wafers. Measured samples fall within 100 and 10^5 (ohm cm). The sensitivity of this method is limited to resistivities less than 10^5 (ohm cm).

Vertical Profilometry

As already demonstrated, the ability to extract vertical profiles in terms of complex conductivity and permittivity is of great potential diagnostic value. We have recently shown that this information can, in many circumstances, be extracted from the frequency dependence of the sample surface impedance measured by the confocal resonator.[8] We have demonstrated, by example, the use of this technique for a number of materials and structures including the conductivity profile of a doped GaAs wafer, the dopant profile of an ultra-shallow implant in Si, and the imaginary conductance profile of a superconducting YBaCuO thin film grown on $LaAlO_3$. In each case, we have compared the results of this non-invasive confocal technique with more commonly used destructive techniques, such as SIMS , and have shown that the difference is insignificant or, in one case, expected.

Conclusions

A technique for corrosion detection and analysis based on mm-wave resonant surface resistance measurements has been presented. While the concept of high frequency cavity measurements for materials analysis is not new, this particular implementation and measurement sequence would appear to be more novel. The incipient detection (before optically observable) of Al, Ti and a steel example have all been discussed. The minimal detectable product thicknesses are all well below 100 nm (10 nm is probably a lower bound) with an accompanying set of data available of trends in both real and imaginary parts of the dielectric constant of the product. Incipient corrosion-related cracks around rivet holes have also been measured with features smaller than 100 μm being detectable. All of these analysis are based on the disruption in the ability to generate RF currents in the sample under test. The power levels are low, the measurements are fast, and the results repeatable to normally within 1% (in terms of surface resistance).

In addition, the results of techniques for chemical sensing using the CR has been described for a wide variety of applications. The sensitivity in terms of complex permittivity is good allowing for reasonable material analysis and the physical resolution is very fine in the vertical direction allowing structures as thin as a few nanometers to be studied. Other experiments in progress include the analysis of the deposition of corrosion inhibitors on Cu, the study of flux on circuit boards and the effectiveness of flux removers, the analysis of growth of dielectrics on semiconductors and the analysis of implantation profiles in semiconductors.

We have also characterized several high resistivity Si wafer samples with respect to their dielectric properties near 100GHz and have developed several techniques, including extensive data analysis, for reducing the results to a form directly comparable to DC transport experiments. We find that the confocal resonator can be used effectively in this application.

References

[1]G. D. Boyd and J. P. Gordon, "Confocal Multimode Resonator for Millimeter Through Optical Wavelength Masers," Bell Sys. Tech. Jour., **40**, pp. 489-508, March 1961.

[2]J. S. Martens, V. M. Hietala, D. S. Ginley, T. E. Zipperian and G. K. G. Hohenwarter, "Confocal resonators for measuring the surface resistance of high temperature superconducting films," Appl. Phys. Lett., **58**, pp. 2543-2545, June 1991.

[3]J. S. Martens, S. M. Garrison, and S. A. Sachtjen, Solid State Tech., **37**, no. 12, 51 (1994).

[4]J. S. Martens, D. S. Ginley, and N. R. Sorensen, "A novel millimeter-wave corrosion detection method," J. Electrochem. Soc. **139**, 2886 (1992).

[5] R. E. Collin, Foundations for microwave engineering (McGraw-Hill, New York, 1966), Chp. 5.

[6]K. E. Lonngren, J. W. Mink, and J. B. Beyer, IEEE Trans. on MTT, MTT-12, 548 (1964).

[7]R. F. Harrington, "Time-Harmonic Electromagnetic Fields," Chps. 2 and 7, McGraw-Hill, New York, (1961).

[8]J.S. Martens *et al* , "Millimeter-wave Confocal Resonator for Vertical Structure Profiling in Semiconducting and Superconducting Materials", 1993 International Microwave Symposium Digest, **15**, pp. 1243-1246, June 1993.

[9]J. S. Martens, T. E. Zipperian, D. S. Ginley, V. M. Hietala, C. P. Tigges, and T. A. Plut, "The effects of processing sequences on the microwave surface resistance of TlCaBaCuO," J. Appl. Phys., **69**, pp. 8268-8271, June 1991.

[10]S. Ramo, J. R. Whinnery, and T. Van Duzer, Fields and Waves in Communication Electronics, pp. 577-580, John Wiley & Sons, New York, 1965.

[11]J.S. Martens, J. B. Beyer, D. S. Ginley, "Microwave Surface Resistance of $YBa_2Cu_3O_{6.9}$ Superconducting Films", Appl. Phys. Lett., **52**, pp. 1822-1824, May 1988.

[12]J. S. Martens, D. S. Ginley, and N. R. Sorensen, "A Novel Millimeter-wave Corrosion Detection Method", J. Electrochem. Soc., Oct. 1992.

[13]T. Van Duzer and C. W. Turner, Principles of Superconductive Devices and Circuits ch. 3, Elsevier, New York, 1981.

APPENDIX A

The Confocal Resonator

For any application, the time and labor saved by pre-characterizing materials and by evaluating failed processed samples is very substantial. An image of surface resistance across a sample surface provides such a characterization. A non-invasive method of measuring surface resistance based on a quasi-optical resonator has been adapted to perform this imaging. The method has been used to routinely characterize 2" and 3" wafers of YBaCuO and TlCaCuO superconductors.

The technique is based on the use of a confocal resonator for surface resistance measurement [2,9]. A diagram of the apparatus is shown in Figure 13. The system is comprised of a spherical mirror positioned above the surface of the sample which together form an open resonant cavity. The open cavity permits the measurement to be non-contact which allows for the use of simple cooling methods (required for superconducting sample) and the movement of either the sample or the mirror for imaging. This resonator may exhibit a very high quality factor allowing for the measurement of materials with very low surface resistance. To determine the resonant frequency (f_o) and the unloaded quality factor (Q), a swept frequency Gunn oscillator is weakly coupled into the resonator and the absorbed power is measured with a dual directional coupler and dual detectors. Alternatively, a network analyzer could be used, however this is not always convenient for reasons of cost or portability.

The measured quality factor is easily related to the surface resistance of the material under test. The quality factor (Q) is define as:

$$Q = \omega_o \frac{energy\ stored}{power\ lost} \tag{A.1}$$

where ω_0 is the angular frequency at resonance. The measured quality factor (Q_t) will represent all losses of the resonator, which for high Q's can be expressed as:

$$\frac{1}{Q_t} = \frac{1}{Q_r} + \frac{1}{Q_c} + \frac{1}{Q_d} \tag{A.2}$$

where Q_r, Q_c, and Q_d are the resonator's ohmic, coupling, and diffraction loss contributions respectively. The coupling loss is effectively removed during the measurement by weak coupling into the resonator, and the diffraction loss is negligible (discussed below). Therefore, the measured quality factor is dominated by the ohmic losses of the spherical reflector and sample ($Q_t \approx Q_r$).

The resonator is assumed to operate in the TEM_{00p} mode which is primarily determined by the coupling method. This mode has the lowest diffraction loss and hence highest quality factor as compared to the other possible modes. Neglecting diffraction losses, assuming Franhauffer propagation, and large dimensions compared to the operating wavelength, the quality factor of the cavity can be easily determined as outlined below.[10] For the analysis, the standing wave within the resonator is divided into two counter-propagating traveling waves. Assuming an energy density U_l per unit length of each wave, the total energy storage is:

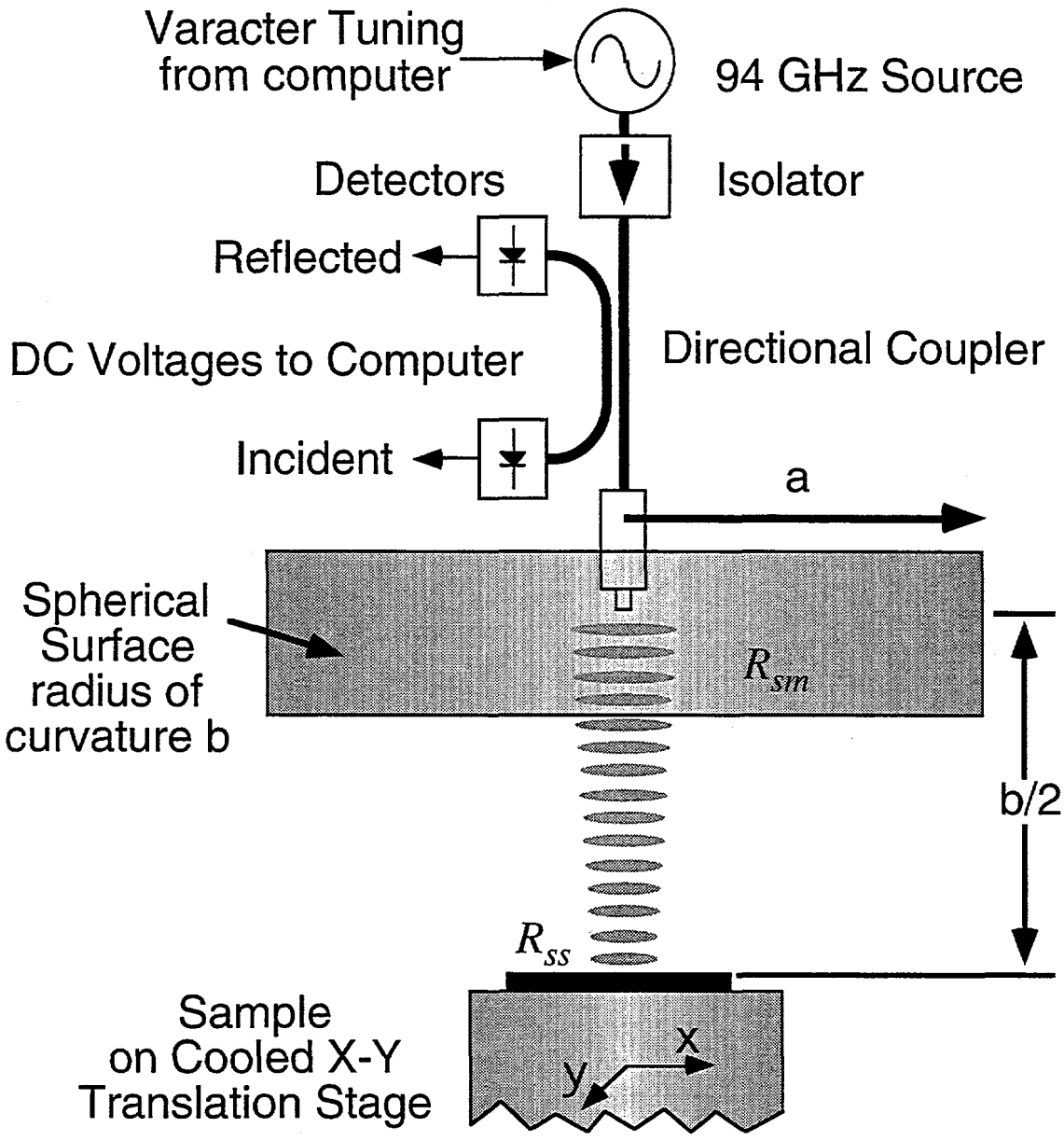

Figure 16. Diagram of the scanning confocal resonator system.

$$Energy\ \ Storage = 2\ U_l d \tag{A.3}$$

in which d is the cavity length ($d=b/2$ for a confocal resonator) and the 2 accounts for both of the counter-traveling waves. The power flow of each wave is U_l c where c is the speed of light. The power loss of a round trip through the resonator can then be expressed as:

$$Power\ Loss = U_l c \left(1 - |\Gamma_s|^2 |\Gamma_m|^2\right) \approx 4 U_l c \left(\frac{R_{ss}}{\eta_o} + \frac{R_{sm}}{\eta_o}\right) \tag{A.4}$$

where $|\Gamma_s|^2$ and $|\Gamma_m|^2$ are the power reflection coefficients at the sample and mirror surfaces, respectively. Equation (A.4) reflects the fact that for highly conductive materials $|\Gamma|^2$ is approximately $4\,R_s/\eta_o$ where R_s is the surface resistance and η_o is the intrinsic impedance of free space ($\approx 377\Omega$). By combining Eqs. (A.1), (A.3), and (A.4), the quality factor becomes :

$$Q_r = \omega \frac{U_l b}{4U_l c\left(\frac{R_{ss}}{\eta_o} + \frac{R_{sm}}{\eta_o}\right)} = \frac{\eta_o}{4} bk \frac{1}{R_{ss} + R_{sm}} \quad . \tag{A.5}$$

This result can be confirmed by the direct integration of the field distributions presented below to determine the total energy storage and power loss on the mirror and sample. In order for this analysis to be valid the *bk* product must be large, that is, the radius of curvature of the mirror must be much larger than the wavelength.

The only design factor in (A.5), other than the mirror surface resistance, is the radius of curvature - wave number product, *bk* . From (A.5), the quality factor linearly depends on *bk*. Therefore, quality factor of the resonator can be increased by increasing the reflector size or by decreasing the operating wavelength (higher frequency). Notice, that little can be done to increase measurement sensitivity; If R_{ss} becomes much smaller in relation to R_{sm}, measurement noise will limit ultimate sensitivity. However, the sensitivity of this technique is still much better as compared to other measurement approaches. For example, with the common technique of end wall replacement[11], the ratio of loss of the material under test to the cavity loss (assuming $R_{ss} = R_{sm}$) is typically about 1/10; whereas with a confocal resonator descibed here, it is approximately 1. Therefore, the confocal resonator is in principle 10 times more sensitive than a typical end wall replacement approach. Since R_{ss} will be measured in relation to R_{sm}, the ultimate measurement accuracy depends on the determination of R_{sm} which, of course, can be determined experimentally by calibrating to a known surface resistance.

Discussion up to this point has focused on the measurement of simple structures, e.g. a metal or superconducting film. More complicated structures can be analyzed as well by studying the frequency dependence of the measured surface impedance. The profile of multi-layer structures can be determined in some circumstances and is the subject of current study.[12]

To elucidate surface resistance imaging, it is necessary to examine the field patterns within the resonator. The electromagnetic solution for the confocal resonator has been extensively studied[1] and for purposes here, a simple Gaussian beam approximation appears adequate. This approximation requires two assumptions: first, the spherical surface of the reflector is approximated as a parabaloid; and secondly, the operating wavelength is assumed much shorter than any of the dimensions of the resonator. Under these conditions, for the TEM_{00p} mode, the electric field can be expressed approximately as:

$$\frac{E(x,y,z)}{E_o} \approx \sqrt{\frac{1}{1+\xi^2}}\, e^{-\left(\frac{k}{1+\xi^2}\frac{r^2}{b}\right)} \cos\left(k\left\{\frac{b}{2}(1+\xi) + \frac{\xi}{1+\xi^2}\frac{r^2}{b}\right\} + \varphi\right) \tag{A.6}$$

in which

$$r^2 = x^2 + y^2,$$

$$\xi = \frac{2z}{b},$$

$$\tan(\varphi) = \frac{1-\xi}{1+\xi},$$

b = the reflector's radius of curvature, and
k = the wavenumber ($2\pi/\lambda$).

The resonant frequency of the cavity is approximately:

$$f_o \approx \frac{c}{b}\left(p + 1/4\right) \tag{A.7}$$

where c is the speed of light, and p is the integer mode number. At the sample (z=0), the beam's radius where the electric field is reduced by 1/e is given by:

$$r_s = \sqrt{\frac{b}{k}} = \sqrt{\frac{b\lambda}{2\pi}} \tag{A.8}$$

which is commonly termed the "spot size". A contour plot of the normalized electric field intensity as given by (A.3) is shown in Figure 14. This plot is shown for the $p = 19$ mode with normalized spatial dimensions. Note that the beam's radius throughout the resonator is on the order of r_s with some focusing of energy on the sample.

As will be discussed in the next section, the loss distribution at the sample is directly related to the magnetic field intensity along the sample's surface. The magnetic field at the sample can be expressed as a simple gaussian spot:

$$|H\|_{z=0} = |H_o|\, e^{-\left(r/r_s\right)^2} \tag{A.9}$$

in which

$$|H_o| = \frac{|E_o|}{\eta_o} \tag{A.10}$$

where H_O is the magnetic field at the center of the probe spot and r is the planar radius from the central axis of the resonator.

The dimensions of the reflector were selected to obtain a reasonable spot size while still maintaining a large enough reflector size to minimize diffraction. The relation for spot size given by (A.8) indicates that decreasing the curvature of radius of the mirror b will decrease the spot size. This is only true within the limit of the present approximations mainly that kb be very large (bk>120 in present design). If b approaches several wavelengths, the reflector's radius a (see Figure 13) will similarly become small and significant diffraction loss will occur which will quickly dominate the sample loss being measured. Increasing the operating frequency will also reduce the spot size. For work with superconductors, increasing the frequency also helps with measurement accuracy and sensitivity, since the superconductor losses increase as ω^2 while the mirror losses increase only as $\omega^{0.5}$.[13] Unfortunately, frequencies higher than the present

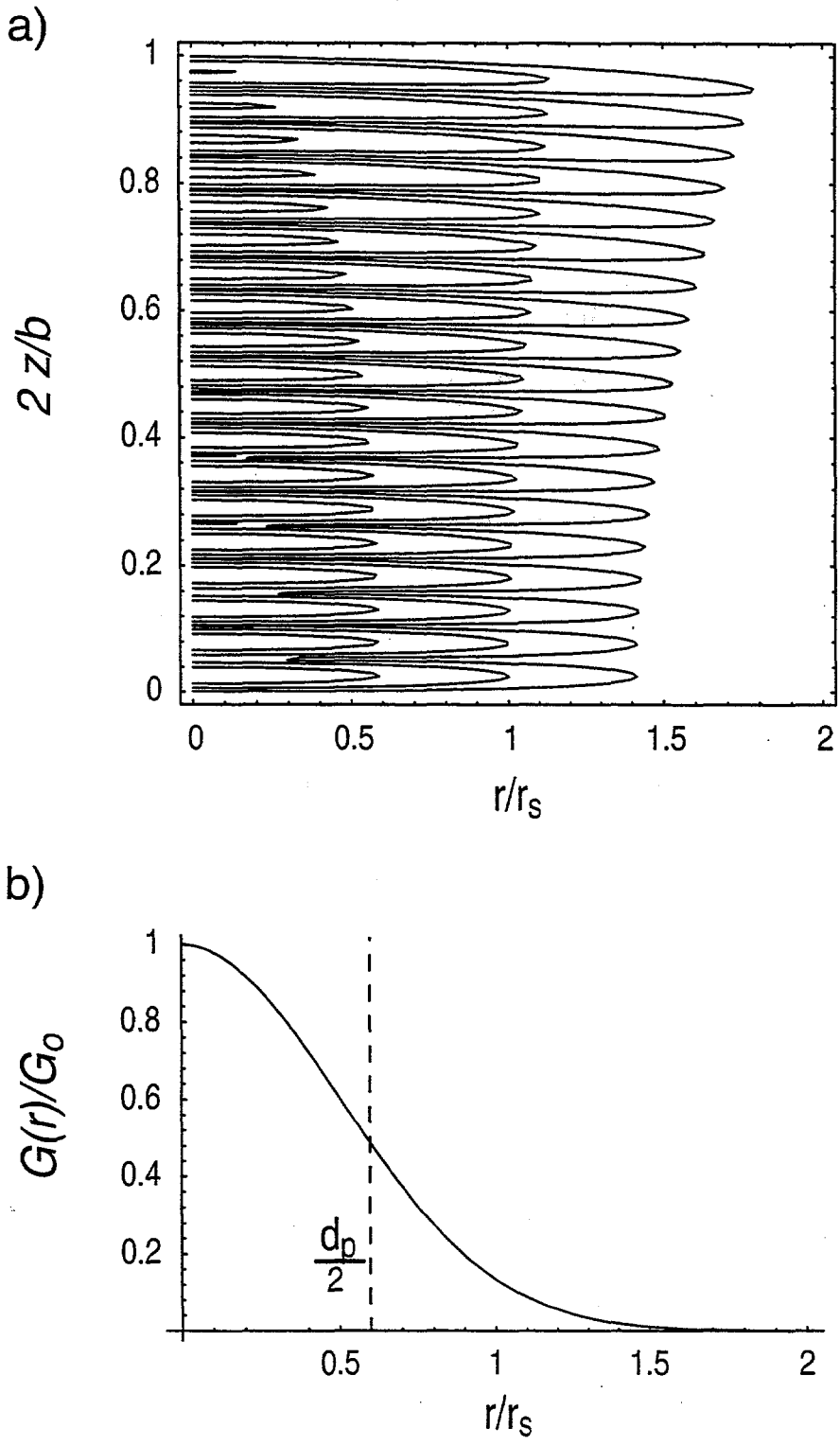

Figure 17. Confocal resonator field distributions. (a) Contour plot of $|E|^2$ as a function of r/r_s and 2 z/b for the $TEM_{0,0,19}$ mode. Coutour groups from left to right are 0.5, e^{-2} and e^{-4}. (b) The normalized sample function G plotted as a function of r/r_s at the sample (z=0).

94 GHz W-band system are somewhat esoteric both for instrumentation as well as for the majority of present day applications. In the present design, $b = 61.4$ mm and $a = 38.4$ mm were selected for the radius of curvature and reflector radius, respectively, with operation in the $p = 19$ mode yielding an operating frequency of 94.05 GHz.

For imaging, it is important to understand the region of the sample contributing to the measurement. With the present mirror design, the spot size, r_s as was defined in (A.5) is about 5.6 mm. This is the radius where the probe field is down by $1/e$ of its central maximum value and therefore is a conservative measure of probe size. Since the quantity being measured depends on an integral of the probe signal's field intensity ($|H|^2$), a more appropriate measure would be the diameter in which half the power is present. From the integration of (A.9), the diameter containing half the probe power is found to be:

$$d_p \approx \sqrt{2\ln(2)}\, r_s \approx 1.18\, r_s \qquad \text{(A.11)}$$

where r_s is given by (A.8). The size scale d_p gives a more realistic estimate of resolution than the spot size r_s. Since the present design yields a diameter of $d_p = 6.6$ mm,which is not reasonable in some applications, methods for enhancing the effective resolution have been explored but are not described in any detail here. These techniques generally use over sampling and non-trivial deconvolution methods for increasing the effective resolution.

DISTRIBUTION:

5	MS	0603	Chris P. Tigges, 01313
5		0603	Tom A. Plut, 01313
5		0874	Vince M. Hietala, 01342
1		4523	Donna Chavez, LDRD
1		0161	John Hohimer, legal
1		9018	Central Technical Files, 8940-2
5		0899	Technical Library, 4414
2		0619	Review and Approval Desk, 12690 For DOE/OSTI